

Article

External Wetting Efficiency in a Three-Phase Fixed Bed Loaded with Porous and Non-Porous Packings

Zhenmin Cheng ^{1,*} , Gang Luo ¹, Yanling Tang ¹, Dan Ling ¹, Zhaoxuan Chen ¹, Peng Liu ¹ and Bo Zhang ²

¹ State Key Laboratory of Chemical Engineering, East China University of Science and Technology, Shanghai 200237, China; gluo123@163.com (G.L.); tangyanling124@163.com (Y.T.); Lingdan0856@126.com (D.L.); chenzhaoxuanqiqi@163.com (Z.C.); liupta@163.com (P.L.)

² State Key Laboratory of Molecular Engineering of Polymers, Department of Macromolecular Science, Fudan University, Shanghai 200438, China; bozhang@fudan.edu.cn

* Correspondence: zmcheng@ecust.edu.cn; Tel.: +86-21-6425-3529; Fax: +86-21-6425-3528

Abstract: Films and rivulets are the two basic forms of dynamic liquid in a three-phase fixed bed (trickle bed), which determines the wetting efficiency of the catalyst. This paper is devoted to the conflicting wetting performance observed between non-porous glass beads and less wettable porous alumina, and a parallel zone model is applied to resolve the complex liquid flow texture. It shows in both cases of glass beads and aluminium pellets, the pressure drop, film flow and rivulet flow fractions all display pronounced multiplicities along with the liquid flow rates in increasing and decreasing branches, although the rivulet flow fraction is reduced to 0 in the liquid decreasing branch started from pulsing flow in both cases. Different from the glass beads, there is almost no wetting efficiency difference for the alumina pellets with respect to liquid flow rate increasing or decreasing, which is in agreement with the dynamic liquid holdup measurements. The liquid is significantly more uniformly distributed over the crosssection in the Al₂O₃ bed since rivulet flow is much reduced than in the case of glass beads.



Citation: Cheng, Z.; Luo, G.; Tang, Y.; Ling, D.; Chen, Z.; Liu, P.; Zhang, B. External Wetting Efficiency in a Three-Phase Fixed Bed Loaded with Porous and Non-Porous Packings. *Processes* **2022**, *10*, 135. <https://doi.org/10.3390/pr10010135>

Academic Editor: Suresh K. Bhatia

Received: 12 December 2021

Accepted: 6 January 2022

Published: 10 January 2022

Publisher's Note: MDPI stays neutral with regard to jurisdictional claims in published maps and institutional affiliations.



Copyright: © 2022 by the authors. Licensee MDPI, Basel, Switzerland. This article is an open access article distributed under the terms and conditions of the Creative Commons Attribution (CC BY) license (<https://creativecommons.org/licenses/by/4.0/>).

Keywords: trickle bed; liquid flow texture; alumina pellets; glass pellets; liquid–solid wetting efficiency

1. Introduction

A three-phase fixed-bed or trickle-bed reactor has been successfully applied in the traditional field of hydrogenation of petroleum fractions [1,2], waste organics oxidation [3,4], etc., and its application in the new area of biomass conversion is growing rapidly, as is shown in sugar hydrogenation [5,6], the hydrodeoxygenation of palm oil [7], aqueous phase reforming [8] and biological methanation [9]. In designing a trickle-bed reactor, the liquid–solid contacting condition, which is characterized by the external wetting efficiency, η_{ce} , is of central importance for the safe and efficient operation of the reactor [10,11]. Since η_{ce} is generally defined as the fraction of catalyst surface covered by flowing liquid, while according to Zimmerman and Ng [12], the flowing liquid includes the film and rivulet, decomposition of the complex liquid flow texture into individual components is key to the determination of wetting efficiency.

In the past few decades, visualization techniques have been developed to provide direct observation of liquid wetting morphology. Lutran et al. [13] reported that the rivulet flow shape varied because of splitting and coalescence with computer-assisted tomography (CAT). The film flow, rather than rivulet flow, prevails in a prewetted bed. Similar results were also observed by Sederman and Gladden [14]; they found the number of rivulets significantly increased with the increase in liquid velocities by using magnetic resonance imaging (MRI). With the high spatial resolution of X-ray CT, van der Merwe et al. [15] proved the dynamic liquid was randomly distributed in the trickle bed in the form of films and rivulets. Recently, Salleh et al. [16] measured the interstitial liquid velocity in a trickle bed reactor by combination of the X-ray Digital Industrial Radiography (DIR) and Particle

Tracking Velocimetry (PTV) techniques. The measured maximum local liquid velocity ranges between 4 and 4.7 times its superficial value, which means different patterns of liquid flow coexist. This shows that despite the complex liquid flow texture being detected qualitatively by the current experimental technology, a quantitative description is not available.

In addition to experimental studies, computational fluid dynamics (CFD) is also widely used to investigate the hydrodynamic characteristics of trickle beds. The film and rivulets can easily be distinguished with fine mesh resolution with the VOF method [17,18]. However, the computational resources required for a VOF method are enormous; therefore, almost all studies are conducted at the micro and mesoscopic scales, and it is difficult to predict the liquid flow texture on the bed scale. As for the Euler–Euler method, which disregards the phase interface of two or more immiscible fluids, it can only be used in pressure drop, liquid holdup, and liquid distribution predictions in a trickle bed [19,20].

As a result, up to now, catalyst external wetting efficiencies are all determined from indirect methods, rather than from the liquid flow texture modeling approach:

- (1) The tracer method [21–25]. The wetting efficiency is defined as the square root of the ratio of the apparent diffusivity of the tracer in a porous particle in a trickle-bed reactor to the diffusivity obtained in a liquid-full reactor. Diffusivities are obtained from the variance of the impulse response of the tracer. Based on a comprehensive theoretical analysis, Julcour-Lebigue et al. [26] demonstrated that under the usual low axial dispersion conditions, factors including the external mass transfer resistance, adsorption of the tracer, flow pattern of the wetted zone, and heterogeneity of wetting on the reactor scale have only a slight effect on the wetting efficiency and, therefore, wetting efficiency can accurately be evaluated from RTD data. The tracer technique has been compared satisfactorily to the direct measurements of partial wetting obtained by dye adsorption [27,28]. In another work by Lappalainen et al. [29], in a hydrodynamic model establishment for wetting efficiency, all wetting efficiency data points were recommended to be obtained from the tracer method, in view of the high reliability of this method.
- (2) The dye adsorption method [27,28,30,31]. Wetting efficiency can be obtained at the pellet scale using this method by colorimetric tracing via dye adsorption. However, this method requires tedious experimental work, since the packing can only be used once and needs to be replaced by a fresh one for the next run. The reactor should be disassembled several times to obtain cross-sectional photographs of the packing.
- (3) The hydrodynamic method. Pironti et al. [32] and Kundu et al. [33] applied the shear stress method for wetting efficiency evaluation by comparing the liquid–solid shear stress times of the specific area in the two-phase flow to that in a liquid-full bed at the same intrinsic liquid and gas velocities. The advantage of this method is that the wetting efficiency can be determined directly from the pressure drop and liquid holdup measurements, which is quite convenient compared to the tracer and colorimetric methods. Its accuracy needs to be improved in view of the remarkable discrepancy from the literature reports. On the other hand, the liquid morphology observation has also been used for the wetting efficiency estimation, as shown in the work of Sederman and Gladden [14]. The authors attempted to obtain the wetting efficiency from the fraction of surface voxels that contain liquid. A wetting efficiency of 0.56 was obtained at a liquid flow rate of $5.8 \text{ mm}\cdot\text{s}^{-1}$ and gas superficial velocity of 66 mm/s. This shows that the MRI method appears to be a very promising tool for obtaining flow features and quantitative analysis.
- (4) The reaction method. This method was initially proposed by comparison of reaction rates in a two-phase operation and in a reactor completely filled with liquid [34,35]. An innovative parallel hydrogenation for the quantification of wetting efficiency in a trickle-bed reactor was introduced by van Houwelingen and Nicol [36]. In this method, the reaction rates of two first-order liquid-limited hydrogenation reactions occurring in parallel were measured under upflow and trickle flow conditions. The

higher conversion in the upflow operation was explained by the complete wetting and better liquid–solid mass transfer characteristics.

The purpose of this work is to clarify the long-held confusion on the conflicting wetting performance observed in non-porous glass beads and porous alumina pellets. It is known that the advancing contact angle of water in the presence of air over glass beads is less than 15° [37], whereas it is more than 70° [38] or 65° [28] over porous alumina pellets. Despite the lower contact angle of water over non-porous glass beads and, thus, greater expected wettability and stronger liquid spreading, contrary results are observed. The less wettable alumina pellets show a better liquid spreading than the glass beads in a non-pretreated bed, and the pretreated bed behaves in the same fashion for these two pellets [39]. To explain this extraordinary phenomenon, Khanna and Nigam [40] and Maiti et al. [38,41] modeled the alumina pellet surface as alternating patches of pores and solid surface. As liquid spreads over the alumina pellets surface, the spreading over the solid surface is very similar to the spreading on a non-porous surface and is governed by the contact angle of the liquid. On the other hand, a liquid-filled pore acts as a completely wetted surface; the saturated pores are thought to act as “attractors” for the moving liquid flow. Consequently, the spreading over the alumina pellets surface is governed by the pore of the surface rather than by the contact angle of the liquid. More recently, with high-resolution gamma ray tomography at a spatial resolution of about 2 mm, Schubert et al. [42] also observed very different hydrodynamic behavior for the non-porous glass beads and porous Al_2O_3 support, that at 100 mm downstream below the top of the packing the dynamic liquid was significantly more uniformly distributed over the cross-section in the Al_2O_3 bed than in the glass bed, which indicates that there is no liquid rivulets in Al_2O_3 bed. It can be assumed that only film flow prevails over the Al_2O_3 packing in the pretreated porous bed. Their finding is consistent with the conclusion of Maiti et al. [38] that the external wetting of the porous catalyst surface can lead to internal wetting due to capillary forces, and the internal wetting further leads to more enhanced external wetting. However, there is no further investigation on this subject. In this work, the assumption of Schubert et al. [42] will be evaluated from the calculation of film flow fractions for the two kinds of packing.

2. Liquid Flow Texture Modeling

Pressure drop and liquid holdup hysteresis indicate the existence of multiple hydrodynamic states in the liquid flow rate’s increasing and decreasing branches. In the liquid flow rate’s increasing branch, it is difficult to realize uniform gas–liquid distribution at low liquid velocity, and the single-phase flow may occur in some parts of bed cross-section. The trickle bed can be classified into a gas zone, a liquid zone, and a two-phase flow zone with the same pressure drop [43]. However, uniform distribution of gas–liquid flow is observed when reaching pulsing flow and tends to persist in the liquid flow’s decreasing branch. The reason is that compared to the dry bed, a smaller liquid velocity is required to maintain the film flow on the already wetted bed.

To predict the liquid flow texture, the parallel zone model by Wang et al. [43] was further developed into a liquid flow texture model by Cheng et al. [44], which is shown in Figure 1.

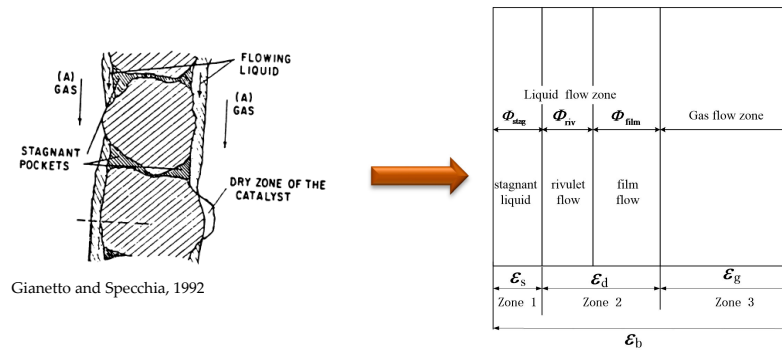


Figure 1. Parallel zone model describing liquid flow texture in a trickle bed [45].

The volumetric fractions of the three liquids are denoted as Φ_{stag} , Φ_{film} and Φ_{riv} , with the total of them equaling 1. In addition, the liquid film zone is controlled by a two-phase flow equation, the stagnant liquid zone by a gas-phase flow equation, and the rivulet zone by a liquid-phase flow equation. Equation (1) is proposed for the prediction of η_{ce} , since it is believed that the contribution of the film is different from the rivulet due to their different morphologies:

$$\eta_{ce} = \Phi_{film}^{\frac{2}{3}} + \Phi_{riv} \tag{1}$$

It was shown that Equation (1) has much better agreement with the empirical correlation of Mills and Duduković [24] than the form of $\eta_{ce} = \Phi_{film} + \Phi_{riv}$.

The variables Φ_{film} and Φ_{riv} are obtained as below:

$$\Phi_{film} = \frac{\varepsilon_{film}}{\varepsilon_{L,d}^*} \tag{2}$$

where $\varepsilon_{L,d}^*$ is the dynamic liquid holdup at the pulsing flow inception point, under which conditions, the bed is completely wetted.

Similar to Equation (2), the fraction of rivulet flow is written as:

$$\Phi_{riv} = \frac{\varepsilon_{L,d} - \varepsilon_{film}}{\varepsilon_{L,d}^*} \tag{3}$$

where $\varepsilon_{L,d}$ denotes the dynamic liquid holdup, which is composed of the contributions from the liquid film and rivulet.

In view of the volumetric conservation of the liquid phase, the fraction of stagnant liquid is therefore obtained:

$$\Phi_{stag} = 1 - \Phi_{film} - \Phi_{riv} \tag{4}$$

The above definition guarantees that $\Phi_{film} + \Phi_{riv} = 1.0$ and $\Phi_{stag} = 0$ under pulsing flow, since $\varepsilon_{L,d} = \varepsilon_{L,d}^*$.

In the following steps, the liquid holdup in the film flow, $\varepsilon_{film,L}$, will be firstly determined, and the two-phase flow equation can be resorted to, as suggested by Sáez and Carbonell [46]:

$$\psi_G = \frac{1}{k_G} \left\{ A \frac{Re_G^*}{Ga_G^*} + B \frac{Re_G^{*2}}{Ga_G^*} \right\} \tag{5}$$

where ψ_G is the dimensionless pressure drop:

$$\psi_G = \frac{1}{\rho_G g} \left(- \frac{\Delta P_G}{\Delta Z} \right) \tag{6}$$

k_G is the gas phase permeability coefficient; Re_G is a modified Reynolds number for the gas defined as $\rho_G u_G d_p / \mu_G (1 - \varepsilon_b)$; $A = 180$ and $B = 1.8$ are the Ergun equation coefficients.

From ψ_G , k_G can be obtained from Equation (5). In general, k_G can be correlated with the gas phase saturation S_G according to Equation (7):

$$k_G = \alpha \cdot S_G^\beta \quad (7)$$

with

$$S_G = 1 - \frac{\varepsilon_L}{\varepsilon_b} \quad (8)$$

The coefficient α and power β in Equation (7) are estimated from a logarithmic plot of k_G against S_G . S_G is the obtained liquid holdup measurements according to Equation (8).

In Equation (7), it is anticipated that as S_G approaches 1.0, k_G should be 1.0 as well. Hence, a large deviation of α from 1 would suggest a poor physical relationship between k_G and S_G . In gas–liquid flow, $\alpha = 1$ means the flow texture is completely in film flow, while a large deviation from 1 means the liquid flow is a mixture of several flow patterns, and the two-phase pressure drop cannot be accurately predicted with the permeability concept of Equation (1).

It should be noted that Equations (5)–(8) are only valid for film flow; therefore, if the correlation Equation (7) is established, S_G will be obtained from k_G , and then ε_L is known from Equation (8). Furthermore, if Equation (7) is obtained under the complete film flow condition, ε_L will be equal to $\varepsilon_{\text{film}}$. On the other hand, if the experiments were conducted under a complex flow texture condition with both the film and rivulet in parallel, the specific ε_L obtained from Equations (7) and (8) will also be equal to $\varepsilon_{\text{film}}$. In this way, $\varepsilon_{\text{film}}$ will be firstly discriminated from the total dynamic liquid holdup ε_L .

In this work, to check the validity of the liquid flow texture-based wetting efficiency formula of Equation (1), the correlation of Mills and Duduković [24] is used as a criterion:

$$\eta_{ce} = \tanh \left[0.664 \text{Re}_L^{0.333} Fr_L^{0.195} We_L^{-0.171} \left(\frac{a_t d_p}{\varepsilon_b^2} \right)^{-0.0615} \right] \quad (9)$$

This correlation was established for the Al_2O_3 pellets, comprehensively correlated by four well-defined dimensionless groups accounting for different properties of the system. The correlation was reported to have a high accuracy with an average error of 0.3% and a standard deviation of 3.5% in a large interval of superficial liquid mass velocity of 0.1 to 1.0 $\text{kg}/(\text{m}^2 \cdot \text{s})$.

3. Experimental Work

The trickle bed reactor was made of a transparent Plexiglass column of 14 cm for the inside diameter and was packed to a height of 1 m. Glass beads of 1.9 mm and alumina pellets of 1.6 mm are used as the packing, with their properties shown in Table 1. Air and deionized water were used as the gas–liquid fluids and all the experiments were conducted under ambient pressure and temperature.

Table 1. Packing characteristics and static liquid holdup.

Packing Material	Shape	d_p /mm	ε_b	ε_s		Exp.-Cal. */Cal.*
				Exp.	Cal.*	
alumina	sphere	1.6	0.361	0.07469	0.04975	50.13%
glass	sphere	1.9	0.368	0.04994	0.04965	0.58%

* Calculated from Equation (10).

According to the theoretical analysis of Equation (7), liquid flow texture with only a pure film is required. It is known that pure film flow cannot be achieved with liquid flow rate starting from low to high. However, when the liquid flow rate is reduced from the pulsing flow transition point, i.e., the upper endpoint of the hysteresis loop, the liquid will be primarily in the form of film due to the vigorous gas–liquid mixing. This leads to a

larger amount of gas–liquid interfacial interactions than the rivulet flow and results in a higher pressure gradient, in turn, sustaining the films and preventing them from reverting back to rivulets [13,47–49].

To make the pressure drop and liquid holdup data reproducible, the bed was first prewetted under gas–liquid pulsing flow conditions for 15 min. After that, the gas and liquid were stopped simultaneously, and the bed was left to drain for 30 min. In each run, the gas flow rate was kept constant, while the liquid flow rate was varied in an increasing mode from 0 to pulsing flow and was then decreased to 0. The liquid holdup under each pair of gas and liquid flow rates was measured by draining the bed, and the pressure drop was measured by pressure transducers.

4. Results and Discussion

4.1. Experimental Results

4.1.1. The Static Liquid Holdup

The measured static liquid holdups for glass and alumina pellets are shown in Table 1, which are 0.0499 for glass and 0.0745 for alumina pellets. Compared with the correlation of Sáez and Carbonell [46], as shown in Equations (10) and (11), the agreement is excellent for the glass beads, while the discrepancy for alumina pellets is up to 50.1% higher than the prediction of Equation (10).

$$\varepsilon_s = \frac{1}{20 + 0.9E\ddot{o}} \quad (10)$$

with

$$E\ddot{o} = \frac{\rho_L g d_p^2 \varepsilon_b^2}{\sigma(1 - \varepsilon_b)} \quad (11)$$

Normally, the static liquid holdup is around 0.05. Although, this can decrease from 0.05 to 0 when $E\ddot{o}$ is varied from 0 to 103, according to Kramer [50].

Nevertheless, a much higher static liquid holdup can be predicted by a different correlation proposed by Sáez et al. [51], which is derived from a system of glass beads from 0.5 to 4 mm in diameter, with water, methanol and kerosene as the liquid phase:

$$\varepsilon_s = \frac{0.11}{1 + E\ddot{o}} \quad (12)$$

This correlation is established for $E\ddot{o}$ from 0.01 to 10, and ε_s up to 0.11 can be obtained if $E\ddot{o}$ is close to 0. Since ρ_L , ε_b and σ do not vary too much, a very low $E\ddot{o}$ can only be obtained in the case of a very small packing diameter. In explaining the packing size effect, Sáez et al. [51] proposed that if the pellets are small enough, the liquid retained in the bed is no longer in the pendular menisci formed at the contact point between the pellets, but in the form of liquid blobs that engulf several pellets. Essentially, a static holdup equal to the bed porosity can be obtained by this mechanism of liquid retention. The packing size effect is also reported by Ortiz-Arroyo et al. [52], who shows that among factors including pellet size, surface tension, liquid density, bed porosity, and sphericity, only pellet size can be regarded as a sensitive one, which would give rise to a high static liquid holdup. As shown in Figure 6a in their paper, ε_s may increase rapidly to 0.14 with the decrease in pellet size in the region of less than 1 mm.

Based on the above analysis, it may be interesting to guess whether the high static liquid holdup for alumina pellets is due to packing size effect. From Equation (12), $E\ddot{o} = 0.476$ is predicted to correspond to $\varepsilon_s = 0.0745$, and the packing diameter d_p is predicted to be 3.32 mm according to Equation (11). Since the actual diameter of 1.6 mm is much smaller than the theoretically predicted packing diameter, packing size is not the reason for the difference between alumina and glass packings. Therefore, the only reasonable reason for the larger static liquid holdup for the alumina pellets is due to the numerous liquid-filled pores over the external surface of the alumina pellets, which provide much stronger adhesive forces than the glass surface to the liquid.

4.1.2. Hysteresis in Dynamic Liquid Holdup

The dynamic liquid holdup $\varepsilon_{L,d}$ was measured for these two pellets under three gas flow rates of 0.065, 0.130 and 0.195 $\text{kg}\cdot\text{m}^{-2}\cdot\text{s}^{-1}$, while the liquid flow rate was varied from 0 to 21.67 $\text{kg}\cdot\text{m}^{-2}\cdot\text{s}^{-1}$ and then decreased to 0. As shown in Figure 2, in all the experimental runs, $\varepsilon_{L,d}$ for the alumina pellets bed is higher by 8% in absolute value than that for the glass spheres. A more obvious difference is found in the hysteresis loops of $\varepsilon_{L,d}$. There is almost no discrepancy between the two branches for the alumina pellets, while it is obvious for the glass spheres at liquid flow rates from 0 to 6.3 $\text{kg}\cdot\text{m}^{-2}\cdot\text{s}^{-1}$, which means the wetting of the glass beads in the liquid flow rate's increasing branch is not as good as that in the decreasing branch, while it is the same for the alumina pellets.

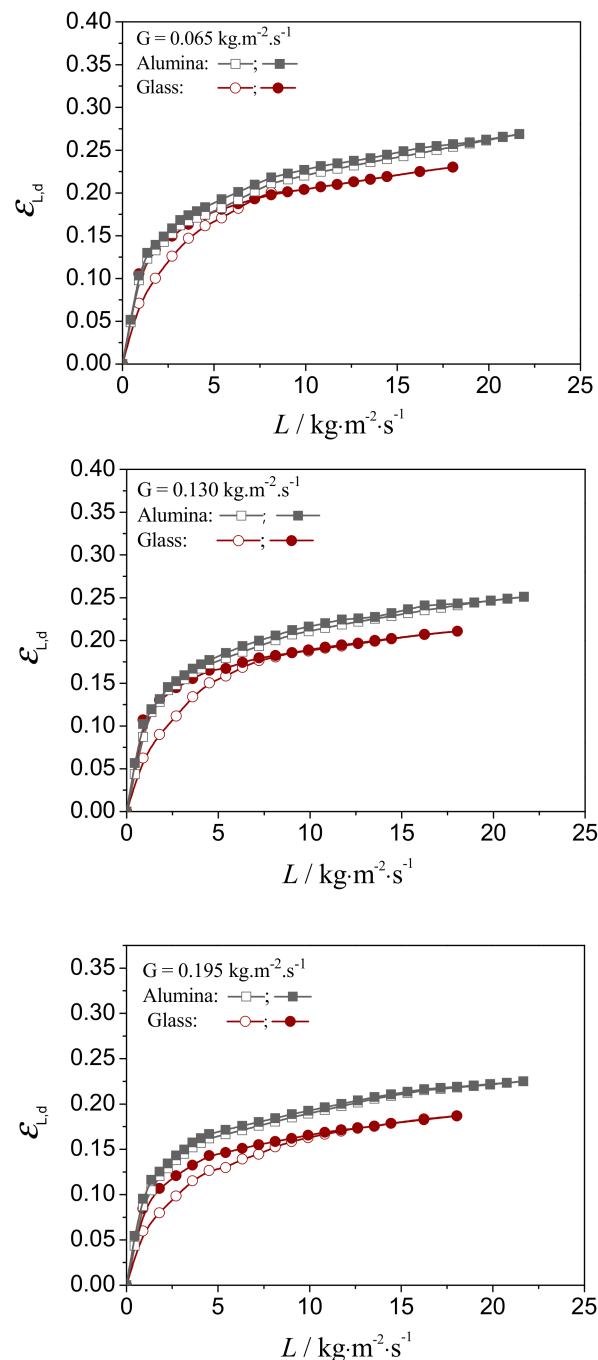


Figure 2. Dynamic liquid holdup measurements for different pellet diameters. \circ, \square —Liquid flow rate increasing; \bullet, \blacksquare —Liquid flow rate decreasing.

4.1.3. Hysteresis in Pressure Drop

Hysteresis loops of pressure drop gradient ($-\Delta P/\Delta Z$) at three gas flow rates versus different liquid flow rate changing paths are shown in Figure 3. The larger pressure drop gradient in the liquid flow rate's decreasing path is due to a larger gas–liquid interfacial area over the packing, since the liquid–solid contacting angle in the two manners of operation is different [48], as a result of the transformation of rivulet flow into film flow [47]. In this work, to transform the rivulet flow entirely into the film flow, the liquid flow rate was increased first to pulsing flow and then decreased inversely.

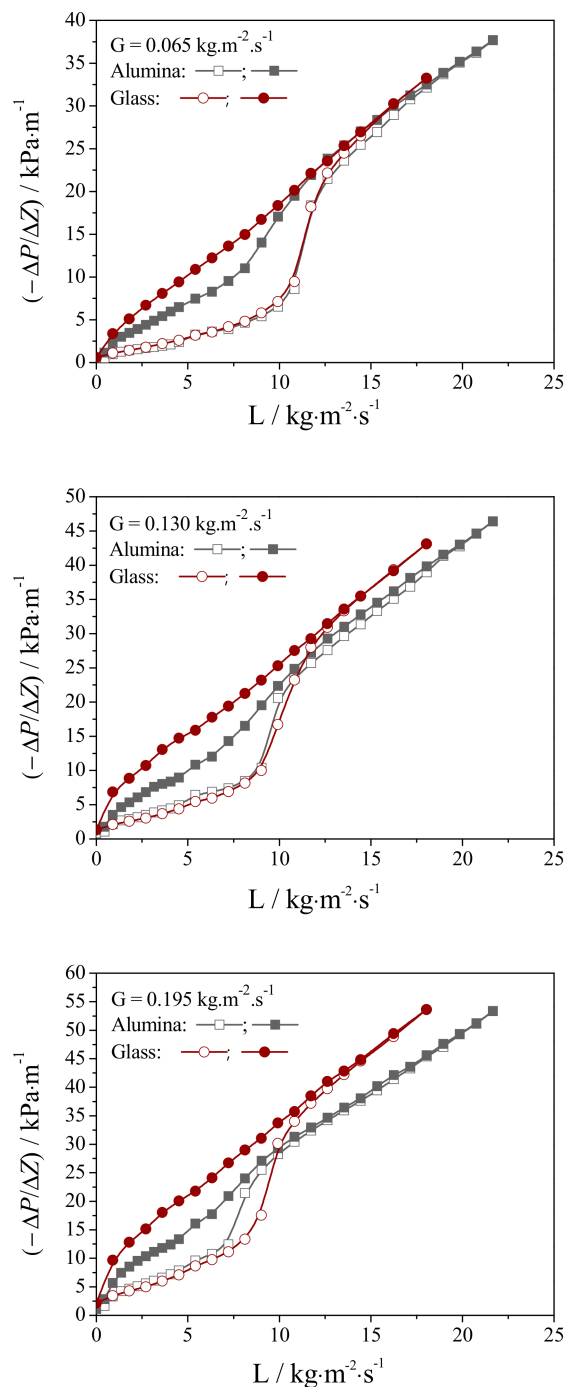


Figure 3. Influence of gas and liquid flow rates on pressure drop hysteresis. \circ , \square —Liquid flow rate increasing; \bullet , \blacksquare —Liquid flow rate decreasing.

It is interesting to find that the lower branch of $(-\Delta P/\Delta Z)$ profiles in the liquid flow rate's increasing runs coincide with each other for the two packings, which means similar gas–liquid and liquid–solid contacting conditions from trickling to pulsing flow are encountered in the two beds. However, the upper branch of $(-\Delta P/\Delta Z)$ in the liquid flow rate's decreasing runs for alumina pellets is shown to be lower than that of glass spheres, which means a reduction in two-phase interaction. Moreover, the shapes of the two profiles are also different: the one for the glass sphere is close to a straight line, while the one for the alumina pellets is much more complicated. The above difference implies that in the glass spheres bed, the liquid–solid contacting state keeps constant, since pressure drop varies linearly with the liquid flow rate, while in the alumina pellets bed, it undergoes a series of changes from film flow in the high interaction region to a mixed flow texture in the low interaction region. Nevertheless, it is shown that an increase in gas flow rate can reduce this trend.

4.2. Modeling Results

4.2.1. Liquid Flow Texture Characterization

It is known that in the trickling flow regime, the solid is contacted with two forms of dynamic liquid: the liquid film and the rivulet. Corresponding to the flow regime transition from trickling flow to pulsing flow, the complex liquid flow texture will be reduced completely into film flow, which provides the opportunity to establish the unique pressure drop relationship with respect to the gas saturation for the film flow, as suggested from Equations (5)–(7).

In Table 2, the parameters of the correlation between k_G and S_G are estimated for the two packings in the liquid flow rate's decreasing loop. This shows that the coefficients are only slightly deviating from 1.0. In comparison, the coefficients for glass beads in the liquid flow rate's increasing branch are in the range of 1.55 to 2.48 [44], which deviates substantially from 1.0.

Table 2. Correlations of the gas phase relative permeability vs. the gas phase saturation in the liquid flow rate's decreasing branch.

Packing Material	$G/\text{kg}\cdot\text{m}^2\cdot\text{s}^{-1}$		
	0.065	0.130	0.195
Alumina	$k_G = 0.92S_G^{2.03}$	$k_G = 0.98S_G^{2.20}$	$k_G = 0.98S_G^{2.55}$
Glass	$k_G = 0.90S_G^{2.99}$	$k_G = 1.01S_G^{3.08}$	$k_G = 1.05S_G^{3.21}$

To check the accuracy of the pressure drop prediction in the film flow regime, the pressure drops in the liquid flow rate's decreasing branch are predicted from the relative permeability correlation given in Table 2. Parity plots of measurements versus the predictions are compared in Figure 4. This shows that the accuracy of the pressure drop prediction is within the $\pm 30\%$ interval, which means the correlation satisfies the liquid film fraction prediction.

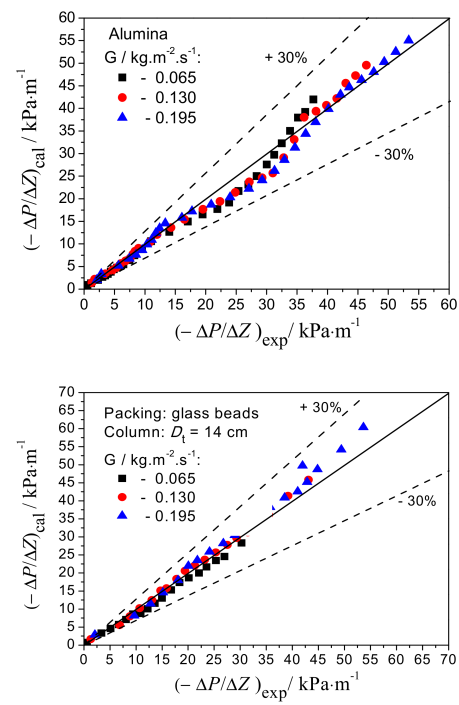


Figure 4. Parity plots of pressure drop measurements versus the predictions.

The wetting condition over the packing surface can be represented by the liquid flow texture in the form of fractions of the stagnant liquid, film flow and rivulet flow, which are shown in Figures 5–7.

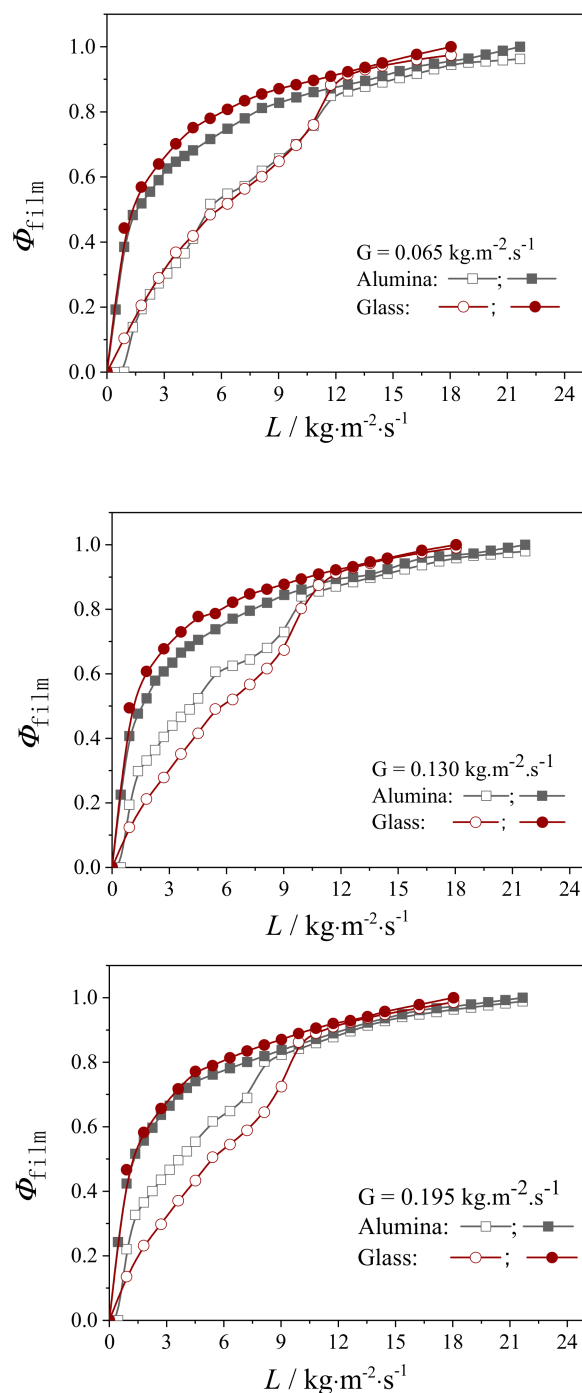


Figure 5. Fraction of film flow over the packing surface. \circ , \square —Liquid flow rate increasing; \bullet , \blacksquare —Liquid flow rate decreasing.

The development of film flow over the two kinds of packing is shown in Figure 5. It is found that at the lowest gas flow rate of $0.065 \text{ kg}\cdot\text{m}^{-2}\cdot\text{s}^{-1}$, there is almost no difference in the film flow fraction Φ_{film} between the alumina and glass pellets. When the gas flow rate is increased to 0.130 and $0.195 \text{ kg}\cdot\text{m}^{-2}\cdot\text{s}^{-1}$, Φ_{film} in the trickling flow regime for the alumina pellets is obviously higher than that of glass beads. This result is consistent with the result of Schubert et al. [42], who observed the dynamic liquid was significantly more uniformly distributed over the cross-section in the Al_2O_3 bed than in the glass bed, which was assumed that only film flow was existing over the Al_2O_3 packing. However, Φ_{film} in

the liquid flow rate's decreasing branch, which corresponds to the film flow regime, shows no difference.

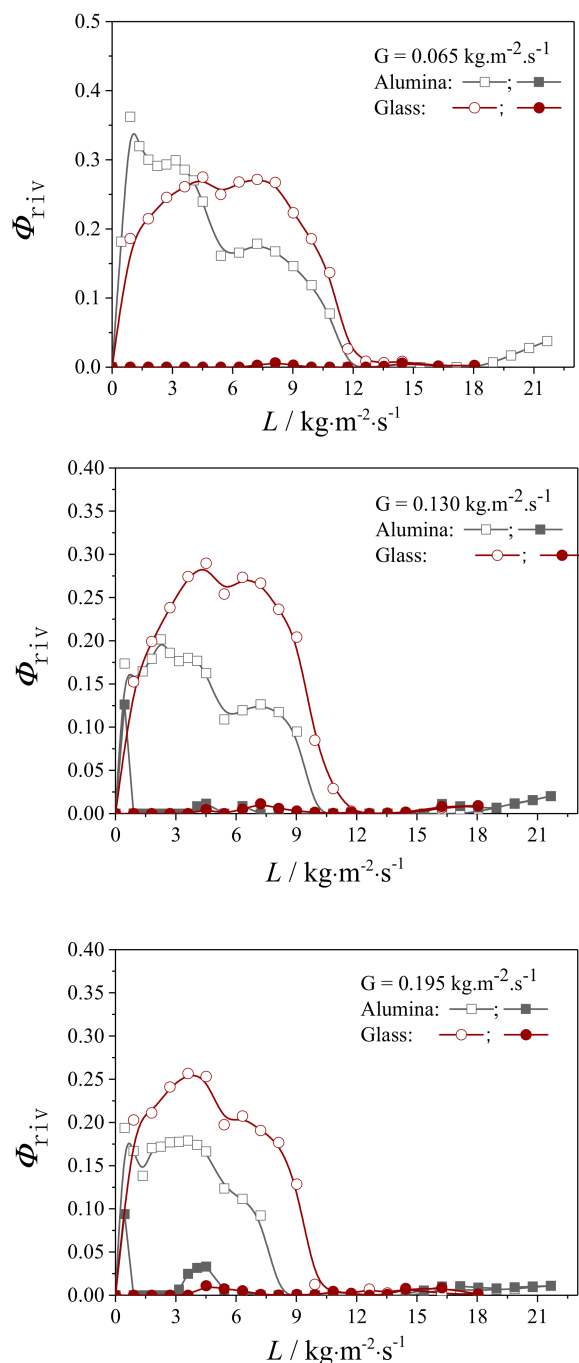


Figure 6. Fraction of rivulet flow over the packing surface. \circ , \square —Liquid flow rate increasing; \bullet , \blacksquare —Liquid flow rate decreasing.

The difference in the liquid flow rate's increasing branch can be explained from the different surface properties of the two pellets. On the porous surface of the alumina pellets, there is a large amount of liquid-filled pores, which tend to adhere liquid droplets. When the surface force cannot counterbalance the droplet weight and the gas friction, the liquid droplet will fall and connect to a lower pore, leading to the formation of a stripe of liquid film. In comparison, the liquid film formation over the glass sphere surface only depends on the liquid–solid surface tension, which is more difficult than the porous surface of alumina. As shown in Figure 5, in the liquid flow rate's decreasing branch, there is

not much difference between the porous and non-porous surface, since both surfaces are covered with liquid film, and hence, no obvious difference in film flow fraction is observed for the two packings; even the liquid flow rate is reduced to a very low value.

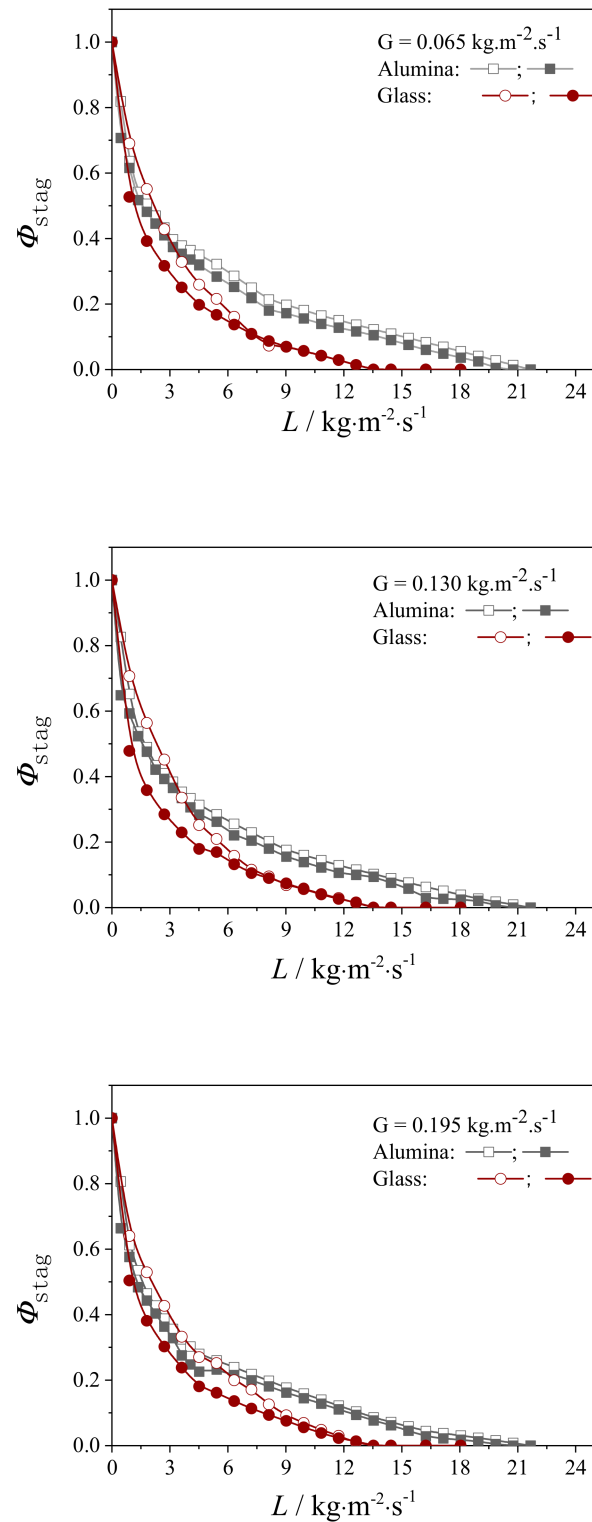


Figure 7. Fraction of stagnant liquid over the packing surface. \circ , \square —Liquid flow rate increasing; \bullet , \blacksquare —Liquid flow rate decreasing.

The importance of pores on the liquid spreading over the substrate surface has been demonstrated by Maiti et al. [41] in Figure 6 of their paper with a perforated steel plate.

They described saturated pores as acting as “attractors” for the moving liquid droplet, i.e., a droplet moving toward the pore is accelerated; on the other hand, a liquid droplet moving away from the pore is held up. The pore acts as accelerator or brake for the droplets. Its acceleration effect results in an increased fractional coverage and wetting efficiency during the increase in liquid flow rate.

A comparison of the fraction of the rivulet flow over the alumina and glass pellets is given in Figure 6. This shows that the fraction of the rivulet flow increases first from 0 to a maximum of 30% over the glass beads and 20% over the alumina pellets, and then it decreases to 0 at a liquid flow rate of about $12.5 \text{ kg}\cdot\text{m}^2\cdot\text{s}^{-1}$, which corresponds to the pulsing flow inception point as indicated from Figure 3. Moreover, since the liquid-saturated pores are favorable for liquid spreading and film formation, there should be less rivulet fraction over the alumina pellets surface than that over the glass pellet surface. This speculation has been verified by the theoretical prediction given in Figure 5, and is consistent with the discussions on the action of pores [38,40,41].

The fractions of stagnant liquid over the alumina pellets and glass beads are presented in Figure 7 with the variation in liquid flow rate. This shows that there is more stagnant liquid fraction over the alumina pellets than over the glass ones, which is consistent with the more static liquid holdup in the alumina bed due to the pinning effect of the pores, since the pores can provide an extra force such as the pinning force in the liquid spreading process [41]. It is found that despite the fact that the fractions of stagnant liquid region over the two kinds of pellet both decrease rapidly with the increase in liquid flow rate, there are still two obvious differences between them. First, it is shown in the case of glass beads that the stagnant liquid region reduces to 0 at a liquid flow rate of $12.5 \text{ kg}\cdot\text{m}^2\cdot\text{s}^{-1}$ with the inception of pulsing flow. However, in the case of alumina pellets, stagnant liquid still exists even in the pulsing flow regime, and it will not disappear until a much larger liquid flow rate as high as $21 \text{ kg}\cdot\text{m}^2\cdot\text{s}^{-1}$ is attained. Secondly, as shown in the case of glass beads, there is a hysteresis in the stagnant liquid fraction, which means there are more stagnant liquids in the liquid flow rate’s increasing branch, while it is less in the decreasing branch, since the packing surface is better wetted. In comparison, there is no difference in the case of alumina pellets, since the operation history does not bring about any difference in the pellet surface properties.

4.2.2. Evaluation on the External Wetting Efficiency

Since the catalyst packing can only be effectively wetted by the liquid film and rivulet flow, the liquid–solid external wetting should be the joint contribution of these two factors. Since the liquid film provides a surface rather than a volume in the liquid–solid external wetting, its contribution is different from the volumetric contribution of rivulet flow. In this regard, a formula such as Equation (1) is proposed.

It is shown from Figure 8 that excellent agreements on external wetting efficiency η_{ce} for alumina pellets are obtained between the liquid flow texture-based model and the correlation of Mills and Duduković [24] at all gas and liquid flow rates. It should be noted that the better agreement at the lowest gas velocity of $0.065 \text{ kg}\cdot\text{m}^2\cdot\text{s}^{-1}$ than at the highest one of $0.195 \text{ kg}\cdot\text{m}^2\cdot\text{s}^{-1}$ is due to the conserved result from the correlation of Mills and Duduković [24], since in this correlation, η_{ce} will not reach 1.0 unless the liquid flow rate is infinitely large. In fact, η_{ce} will become 1.0 once the pulsing flow regime is reached. In this regard, the prediction obtained from this work seems to be more reasonable.

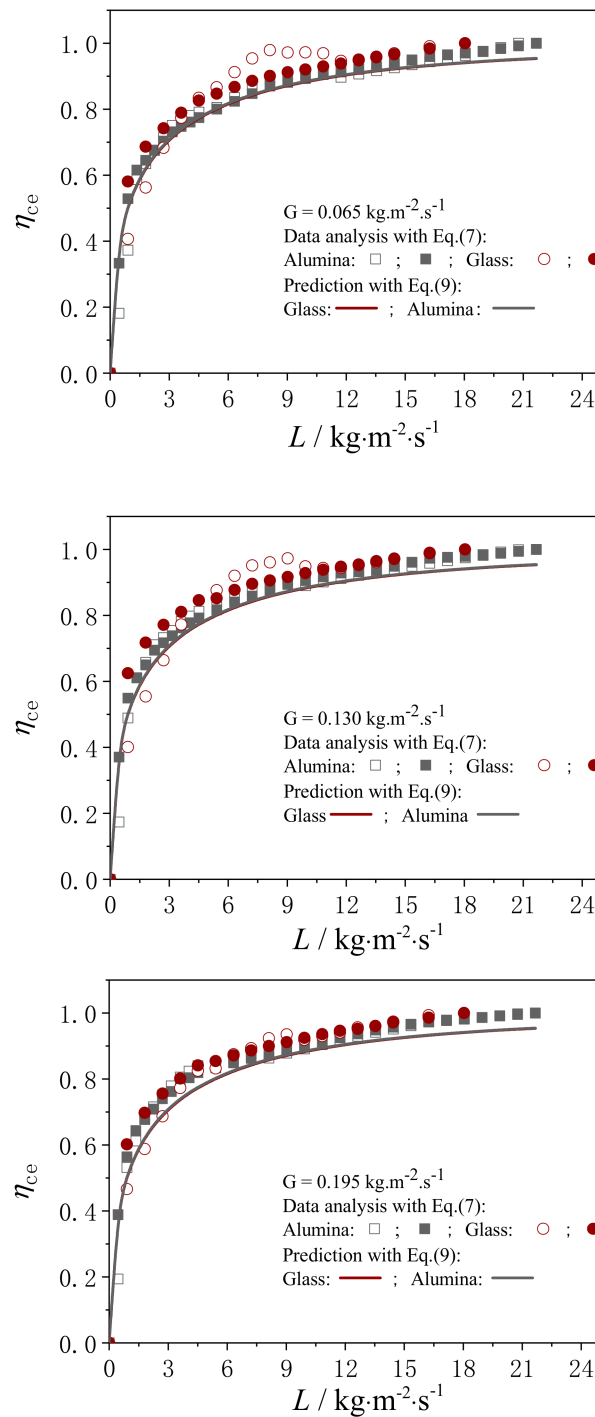


Figure 8. Prediction of liquid–solid wetting efficiency. ○, □—Liquid flow rate increasing; ●, ■—Liquid flow rate decreasing.

Moreover, it is shown in the case of glass beads that the values of η_{ce} in the liquid flow rate's increasing and decreasing branches are different, which is most obvious at the lowest gas flow rate of $0.065 \text{ kg}\cdot\text{m}^{-2}\cdot\text{s}^{-1}$, since the wetting conditions of the packing surface are different in the two operating branches. In comparison, there is no difference in η_{ce} for the alumina pellets, since the same wetting condition over the packing surface is kept before and after the pulsing flow. In view of the same film flow-covered surface of the glass beads and the alumina pellets in the liquid flow rate's decreasing branch, the same wetting efficiency ought to be reached, which is confirmed by the model prediction as shown in Figure 8.

5. Conclusions

From the flow texture modeling approach, it becomes possible to identify the wetting condition of a catalyst bed from the fractions of the film flow, rivulet flow, and stagnant liquid at specific gas and liquid flow rates. It shows that despite the wettability of the alumina pellets surface being much lower than that of glass, as evidenced from the liquid–solid contact angle over alumina pellets of about 70° while it is less than 15° over the glass surface, the alumina pellets still exhibit almost the same wetting efficiency as the glass pellets. Due to the presence of pores, it is not only favorable to the formation of film flow but also to the stabilization of stagnant liquid. Different from the glass beads, there is no multiplicity in dynamic liquid holdup and wetting efficiency for the alumina pellets, since the wetting condition of the alumina pellets surface is primarily influenced by the pores rather than by the external environment. The flow texture analysis result verifies the assumptions by Maiti et al. [38] and Schubert et al. [42].

Author Contributions: Conceptualization, Z.C. (Zhenmin Cheng); methodology, Z.C. (Zhenmin Cheng); investigation, D.L., Z.C. (Zhaoxuan Chen), G.L., Y.T., P.L., B.Z.; data curation, G.L.; writing—original draft preparation, Z.C. (Zhenmin Cheng); writing—review and editing, Y.T.; supervision, Z.C. (Zhenmin Cheng). All authors have read and agreed to the published version of the manuscript.

Funding: The authors are grateful to the financial support from the National Key R&D Program of China (No. 2019YFC1906705) and the National Natural Science Foundation of China (No. 21676085).

Institutional Review Board Statement: Not applicable.

Informed Consent Statement: Not applicable.

Data Availability Statement: All data collected in this study are contained within the article.

Conflicts of Interest: The authors declare no conflict of interest.

Nomenclature

Symbols

a_t	packing external surface area per unit volume of reactor
A, B	Ergun equation coefficients, defined in Equation (1)
d_p	packing diameter, m
$E\ddot{o}$	Eötvös number, defined in Equation (11)
f_w	Wetting fraction of the packing surface
g	gravitational acceleration, $9.81 \text{ m}\cdot\text{s}^{-2}$
G	gas flow rate, $\text{kg}\cdot\text{m}^{-2}\cdot\text{s}^{-1}$
Ga	Galileo number, $\rho^2 g d_p^3 / \mu^2$
Ga^*	modified Galileo number, $\rho^2 g d_p^3 \varepsilon_b^3 / \mu^2 (1 - \varepsilon_b)^3$
k	relative permeability
L	liquid flow rate, $\text{kg}\cdot\text{m}^{-2}\cdot\text{s}^{-1}$
P	Pressure, $\text{N}\cdot\text{m}^{-2}$
Re	Reynolds number, $\rho u d_p / \mu$
Re^*	modified Reynolds number, $\rho u d_p / \mu (1 - \varepsilon_b)$
S	saturation degree, degree in Equation (4)
u	superficial velocity, $\text{m}\cdot\text{s}^{-1}$
Z	axial distance, m

Greek letters

α	coefficient in Equation (3)
β	exponent in Equation (3)
ε	porosity or holdup
ρ	density, $\text{kg}\cdot\text{m}^{-3}$
σ	surface tension, $\text{N}\cdot\text{m}^{-1}$

Φ	volumetric fraction, defined in Equation (5)
η	wetting efficiency
μ	viscosity, Pa·s
ψ	dimensionless pressure drop, defined in Equation (2)
Subscripts	
b	the bed averaged
ce	contacting efficiency
p	packing
L	liquid phase
G	gas phase
film	film flow
riv	rivulet flow
s	static liquid
stag	stagnant liquid

References

- Mary, G.; Esmaeili, A.; Chaouki, J. Simulation of the Selective Hydrogenation of C3-Cut in the Liquid Phase. *Int. J. Chem. React. Eng.* **2016**, *14*, 859–874. [[CrossRef](#)]
- Guan, D.; Chen, Z.; Chen, X.; Zhang, Y.; Qi, Q.; Shi, Q.; Zhao, S.; Xu, C.; Zhang, L. Molecular-level heavy petroleum hydrotreating modeling and comparison with high-resolution mass spectrometry. *Fuel* **2021**, *297*, 120792. [[CrossRef](#)]
- Mohammed, A.E.; Jarullah, A.T.; Ghenni, S.A.; Mujtaba, I.M. Optimal design and operation of an industrial three phase reactor for the oxidation of phenol. *Comput. Chem. Eng.* **2016**, *94*, 257–271. [[CrossRef](#)]
- Kasperczyk, D.; Urbaniec, K.; Barbusinski, K.; Rene, E.R.; Colmenares-Quintero, R.F. Application of a compact trickle-bed bioreactor for the removal of odor and volatile organic compounds emitted from a wastewater treatment plant. *J. Environ. Manag.* **2019**, *236*, 413–419. [[CrossRef](#)] [[PubMed](#)]
- Russo, V.; Kilpiö, T.; Di Serio, M.; Tesser, R.; Santacesaria, E.; Murzin, D.Y.; Salmi, T. Dynamic non-isothermal trickle bed reactor with both internal diffusion and heat conduction: Sugar hydrogenation as a case study. *Chem. Eng. Res. Des.* **2015**, *102*, 171–185. [[CrossRef](#)]
- Schubert, M.; Kost, S.; Lange, R.; Salmi, T.; Haase, S.; Hampel, U. Maldistribution susceptibility of monolith reactors: Case study of glucose hydrogenation performance. *AIChE J.* **2016**, *62*, 4346–4364. [[CrossRef](#)]
- Srifa, A.; Faungnawakij, K.; Itthibenchapong, V.; Assabumrungrat, S. Roles of monometallic catalysts in hydrodeoxygenation of palm oil to green diesel. *Chem. Eng. J.* **2015**, *278*, 249–258. [[CrossRef](#)]
- Aho, A.; Rosales, C.; Eränen, K.; Salmi, T.; Murzin, D.Y.; Grénman, H. Biohydrogen from dilute side streams-Influence of reaction conditions on the conversion and selectivity in aqueous phase reforming of xylitol. *Biomass-Bioenergy* **2020**, *138*, 105590. [[CrossRef](#)]
- Thema, M.; Weidlich, T.; Kaul, A.; Böllmann, A.; Huber, H.; Bellack, A.; Karl, J.; Sterner, M. Optimized biological CO₂-methanation with a pure culture of thermophilic methanogenic archaea in a trickle-bed reactor. *Bioresour. Technol.* **2021**, *333*, 125135. [[CrossRef](#)]
- Hickman, D.A.; Degenstein, J.C.; Ribeiro, F.H. Fundamental principles of laboratory fixed bed reactor design. *Curr. Opin. Chem. Eng.* **2016**, *13*, 1–9. [[CrossRef](#)]
- Hickman, D.A.; Holbrook, M.T.; Mistretta, S.; Rozeveld, S.J. Successful Scale-up of an Industrial Trickle Bed Hydrogenation Using Laboratory Reactor Data. *Ind. Eng. Chem. Res.* **2013**, *52*, 15287–15292. [[CrossRef](#)]
- Zimmerman, S.P.; Ng, K.M. Liquid distribution in trickling flow trickle-bed reactors. *Chem. Eng. Sci.* **1986**, *41*, 861–866. [[CrossRef](#)]
- Lutran, P.G.; Ng, K.M.; Delikat, E.P. Liquid distribution in trickle-beds. An experimental study using computer-assisted tomography. *Ind. Eng. Chem. Res.* **1991**, *30*, 1270–1280. [[CrossRef](#)]
- Sederman, A.J.; Gladden, L.F. Magnetic resonance imaging as a quantitative probe of gas-liquid distribution and wetting efficiency in trickle-bed reactors. *Chem. Eng. Sci.* **2001**, *56*, 2615–2628. [[CrossRef](#)]
- Van der Merwe, W.; Nicol, W.; de Beer, F. Trickle flow distribution and stability by X-ray radiography. *Chem. Eng. J.* **2007**, *132*, 47–59. [[CrossRef](#)]
- Salleh, K.A.M.; Lee, H.K.; Al-Dahhan, M.H. Studying local liquid velocity in liquid-solid packed bed using the newly developed X-ray DIR technique. *Flow Meas. Instrum.* **2015**, *42*, 1–5. [[CrossRef](#)]
- Solomenko, Z.; Haroun, Y.; Fourati, M.; Larachi, F.; Boyer, C.; Augier, F. Liquid spreading in trickle-bed reactors: Experiments and numerical simulations using Eulerian-Eulerian two-fluid approach. *Chem. Eng. Sci.* **2015**, *126*, 698–710. [[CrossRef](#)]
- Markthaler, S.; Plankenbühler, T.; Weidlich, T.; Neubert, M.; Karl, J. Numerical simulation of trickle bed reactors for biological methanation. *Chem. Eng. Sci.* **2020**, *226*, 115847. [[CrossRef](#)]
- Lopes, R.J.G.; de Sousa, V.S.L.; Quinta-Ferreira, R.M. Numerical simulation of reactive pulsing flow for the catalytic wet oxidation in TBR using a VOF technique. *AIChE J.* **2012**, *58*, 493–504. [[CrossRef](#)]
- Bouras, H.; Haroun, Y.; Bodziony, F.F.; Philippe, R.; Fongarland, P.; Augier, F. Use of CFD for pressure drop, liquid saturation and wetting predictions in trickle bed reactors for different catalyst particle shapes. *Chem. Eng. Sci.* **2021**, *249*, 117315. [[CrossRef](#)]
- Schwartz, J.G.; Weger, E.; Duduković, M.P. A new tracer method for determination of liquid-solid contacting efficiency in trickle-bed reactors. *AIChE J.* **1976**, *22*, 894–904. [[CrossRef](#)]

22. Colombo, A.J.; Baldi, G.; Sicardi, S. Solid-liquid contacting effectiveness in trickle bed reactors. *Chem. Eng. Sci.* **1976**, *31*, 1101–1108. [[CrossRef](#)]
23. El-Hisnawi, A.A.; Duduković, M.P.; Mills, P.L. Trickle-Bed Reactors: Dynamic Tracer Tests, Reaction Studies, and Modeling of Reactor Performance. In *Chemical Reaction Engineering*; American Chemical Society: Boston, MA, USA, 1982; Volume 196, pp. 421–440.
24. Mills, P.L.; Dudukovic, M.P. Evaluation of liquid-solid contacting in trickle-bed reactors by tracer methods. *AIChE J.* **1981**, *27*, 893–904. [[CrossRef](#)]
25. Ring, Z.E.; Missen, R.W. Trickle-bed reactors: Tracer study of liquid holdup and wetting efficiency at high temperature and pressure. *Can. J. Chem. Eng.* **1991**, *69*, 1016–1020. [[CrossRef](#)]
26. Julcour-Lebigue, C.; Baussaron, L.; Delmas, H.; Wilhelm, A.-M. Theoretical analysis of tracer method for the measurement of wetting efficiency. *Chem. Eng. Sci.* **2007**, *62*, 5374–5379. [[CrossRef](#)]
27. Baussaron, L.; Julcour-Lebigue, C.; Wilhelm, A.-M.; Boyer, C.; Delmas, H. Partial Wetting in Trickle Bed Reactors: Measurement Techniques and Global Wetting Efficiency. *Ind. Eng. Chem. Res.* **2007**, *46*, 8397–8405. [[CrossRef](#)]
28. Baussaron, L.; Julcour-Lebigue, C.; Wilhelm, A.-M.; Delmas, H.; Boyer, C. Wetting topology in trickle bed reactors. *AIChE J.* **2007**, *53*, 1850–1860. [[CrossRef](#)]
29. Lappalainen, K.; Alopaeus, V.; Manninen, M.; Aittamaa, J. Improved Hydrodynamic Model for Wetting Efficiency, Pressure Drop, and Liquid Holdup in Trickle-Bed Reactors. *Ind. Eng. Chem. Res.* **2008**, *47*, 8436–8444. [[CrossRef](#)]
30. Van Houwelingen, A.J.; Sandrock, C.; Nicol, W. Particle wetting distribution in trickle-bed reactors. *AIChE J.* **2006**, *52*, 3532–3542. [[CrossRef](#)]
31. Julcour-Lebigue, C.; Augier, F.; Maffre, H.; Wilhelm, A.-M.; Delmas, H. Measurements and Modeling of Wetting Efficiency in Trickle-Bed Reactors: Liquid Viscosity and Bed Packing Effects. *Ind. Eng. Chem. Res.* **2009**, *48*, 6811–6819. [[CrossRef](#)]
32. Pironti, F.; Mizrahi, D.; Acosta, A.N.; González-Mendizabal, D. Liquid–solid wetting factor in trickle-bed reactors: Its determination by a physical method. *Chem. Eng. Sci.* **1999**, *54*, 3793–3800. [[CrossRef](#)]
33. Kundu, A.; Nigam, K.D.P.; Verma, R.P. Catalyst wetting characteristics in trickle-bed reactors. *AIChE J.* **2003**, *49*, 2253–2263. [[CrossRef](#)]
34. Satterfield, C.N. Trickle-bed reactors. *AIChE J.* **1975**, *21*, 209–228. [[CrossRef](#)]
35. Morita, S.; Smith, J.M. Mass Transfer and Contacting Efficiency in a Trickle-Bed Reactor. *Ind. Eng. Chem. Fund.* **1978**, *17*, 113–120. [[CrossRef](#)]
36. Van Houwelingen, A.J.; Nicol, W. Parallel hydrogenation for the quantification of wetting efficiency and liquid-solid mass transfer in a trickle-bed reactor. *AIChE J.* **2011**, *57*, 1310–1319. [[CrossRef](#)]
37. Adamsom, A.; Gast, A. *Physical Chemistry of Surfaces*, 6th ed.; Wiley: New York, NY, USA, 1997.
38. Maiti, R.N.; Khanna, R.; Sen, P.K.; Nigam, K.D.P. Enhanced liquid spreading due to porosity. *Chem. Eng. Sci.* **2004**, *59*, 2817–2820. [[CrossRef](#)]
39. Ravindra, P.V.; Rao, D.P.; Rao, M.S. Liquid Flow Texture in Trickle-Bed Reactors: An Experimental Study. *Ind. Eng. Chem. Res.* **1997**, *36*, 5133–5145. [[CrossRef](#)]
40. Khanna, R.; Nigam, K.D.P. Partial wetting in porous catalysts: Wettability and wetting efficiency. *Chem. Eng. Sci.* **2002**, *57*, 3401–3405. [[CrossRef](#)]
41. Maiti, R.N.; Arora, R.; Khanna, R.; Nigam, K.D.P. The liquid spreading on porous solids: Dual action of pores. *Chem. Eng. Sci.* **2005**, *60*, 6235–6239. [[CrossRef](#)]
42. Schubert, M.; Hessel, G.; Zippe, C.; Lange, R.; Hampel, U. Liquid flow texture analysis in trickle bed reactors using high-resolution gamma ray tomography. *Chem. Eng. J.* **2008**, *140*, 332–340. [[CrossRef](#)]
43. Wang, R.; Mao, Z.-S.; Chen, J. Experimental and theoretical studies of pressure drop hysteresis in trickle bed reactors. *Chem. Eng. Sci.* **1995**, *50*, 2321–2328. [[CrossRef](#)]
44. Cheng, Z.; Kong, X.; Zhu, J.; Wang, Z.; Jin, J.; Huang, Z. Hydrodynamic modeling on the external liquid–solid wetting efficiency in a trickling flow reactor. *AIChE J.* **2013**, *59*, 283–294. [[CrossRef](#)]
45. Gianetto, A.; Specchia, V. Trickle-bed reactors: State of art and perspectives. *Chem. Eng. Sci.* **1992**, *47*, 3197–3213. [[CrossRef](#)]
46. Sáez, A.E.; Carbonell, R.G. Hydrodynamic parameters for gas-liquid cocurrent flow in packed beds. *AIChE J.* **1985**, *31*, 52–62. [[CrossRef](#)]
47. Christensen, G.; McGovern, S.J.; Sundaresan, S. Cocurrent downflow of air and water in a two-dimensional packed column. *AIChE J.* **1986**, *32*, 1677–1689. [[CrossRef](#)]
48. Levec, J.; Grosser, K.; Carbonell, R.G. The hysteretic behavior of pressure drop and liquid holdup in trickle beds. *AIChE J.* **1988**, *34*, 1027–1030. [[CrossRef](#)]
49. Chu, C.F.; Ng, K.M. Model for pressure drop hysteresis in trickle-beds. *AIChE J.* **1989**, *35*, 1365–1369. [[CrossRef](#)]
50. Kramer, G.J. Static liquid hold-up and capillary rise in packed beds. *Chem. Eng. Sci.* **1998**, *53*, 2985–2992. [[CrossRef](#)]
51. Sáez, A.E.; Yépez, M.M.; Cabrera, C.; Soria, E.M. Static liquid holdup in packed beds of spherical particles. *AIChE J.* **1991**, *37*, 1733–1736. [[CrossRef](#)]
52. Ortiz-Arroyo, A.; Larachi, F.Ç.; Iliuta, I. Method for inferring contact angle and for correlating static liquid hold-up in packed beds. *Chem. Eng. Sci.* **2003**, *58*, 2835–2855. [[CrossRef](#)]